

Synthesis of calcium orthocarbonate, Ca_2CO_4 -*Pnma* at *P-T* conditions of Earth's transition zone and lower mantle

JANNES BINCK^{1,*†}, DOMINIQUE LANIEL², LKHAMSUREN BAYARJARGAL¹, SAIANA KHANDARKHAEVA³,
TIMOFEY FEDOTENKO², ANDREY ASLANDUKOV², KONSTANTIN GLAZYRIN⁴, VICTOR MILMAN⁵,
STELLA CHARITON⁶, VITALI B. PRAKAPENKA⁶, NATALIA DUBROVINSKAIA², LEONID DUBROVINSKY³,
AND BJÖRN WINKLER¹

¹Institut für Geowissenschaften, Goethe-Universität Frankfurt, Altenhöferallee 1, 60438 Frankfurt am Main, Germany

²Laboratory of Crystallography, University of Bayreuth, 95440 Bayreuth, Germany

³Bayerisches Geoinstitut, University of Bayreuth, 95440, Bayreuth, Germany

⁴Photon Science, Deutsches Elektronen-Synchrotron, Notkestrasse 85, 22607, Hamburg, Germany

⁵BIOVIA Dassault Systèmes, 334 Science Park, Cambridge CB4 0WN, U.K.

⁶Center for Advanced Radiation Sources, The University of Chicago, Chicago, Illinois 60637, U.S.A.

ABSTRACT

We show, by single-crystal diffraction studies in laser-heated diamond-anvil cells, that Ca_2CO_4 orthocarbonate, which contains CO_4^{4-} tetrahedra, can be formed already at ~20 GPa at ~1830 K, i.e., at much lower pressures than other carbonates with sp^3 -hybridized carbon. Ca_2CO_4 can also be formed at ~89 GPa and ~2500 K. This very broad *P-T* range suggests the possible existence of Ca_2CO_4 in the Earth's transition zone and in most of the lower mantle. Raman spectroscopy shows the typical bands associated with tetrahedral CO_4^{4-} -groups. DFT-theory based calculations reproduce the experimental Raman spectra and indicate that at least in the athermal limit the phase assemblage of $\text{Ca}_2\text{CO}_4 + 2\text{SiO}_2$ is more stable than $2\text{CaSiO}_3 + \text{CO}_2$ at high pressures.

Keywords: Carbonate, Ca_2CO_4 , structure, X-ray diffraction, Raman spectroscopy, density functional theory; Volatile Elements in Differentiated Planetary Interiors

INTRODUCTION

Carbonates play a crucial role in the long-term global carbon cycle as they contain ~60–70% of the carbon present on Earth's surface and in its crust (Hirschmann 2018; McKenzie et al. 2016; Ridgwell 2005; Wallmann 2001). As carbonates are partly incorporated into oceanic lithosphere, they may be transported into the deep mantle via subduction (Clift 2017; Kelemen and Manning 2015; McKenzie et al. 2016). Models propose a carbon influx on the order of several tens of megatons per year, which is mainly due to the contribution of carbonate sediments and altered carbonate oceanic crust (Hirschmann 2018; Kelemen and Manning 2015). Within the last two decades, several studies showed that all major carbonates, such as CaCO_3 (Bayarjargal et al. 2018), MgCO_3 (Binck et al. 2020b), FeCO_3 (Cerantola et al. 2017), and $\text{CaMg}(\text{CO}_3)_2$ (Binck et al. 2020a; Merlini et al. 2017), may be stable at the *P-T* conditions of the Earth's mantle, while displaying a variety of different high *P-T* structures (e.g., Binck et al. 2020a; Cerantola et al. 2017; Chariton et al. 2020; Merlini et al. 2017; Gavryushkin et al. 2017; Ono et al. 2007). It has been proposed that carbonates in contact with mantle silicates and metals in the deep Earth are reduced and, depending on the stage of reduction, form metal carbides, or diamonds (Palyanov et al. 2013; Rohrbach and Schmidt 2011; Stagno et al. 2011, 2013). However, carbonate inclusions in diamonds originating from the deep mantle offer direct evidence for the presence of oxidized carbon in the form of

carbonates in at least some regions of the mantle (Brenker et al. 2007; Kaminsky et al. 2016). Cold oxidized subducting slabs with slow reaction kinetics are believed to provide suitable conditions for hosting carbonates even at depths of the lower mantle (Maeda et al. 2017; Martirosyan et al. 2016; Walter et al. 2011).

A recent remarkable discovery are carbonates, in which sp^3 -hybridization of carbon leads to the formation of CO_4^{4-} tetrahedra instead of triangular sp^2 -hybridized CO_3^{2-} -groups (Binck et al. 2020b; Boulard et al. 2011, 2012, 2015; Cerantola et al. 2017; Merlini et al. 2015, 2017; Lobanov et al. 2017). It is now of great interest to determine whether carbonates with sp^3 -hybridized carbon form solid solutions with their silicate analogs and thus provide an alternative major host of carbon in the deeper mantle regions. Up to now, carbonates with CO_4 -groups were synthesized at pressures >70 GPa, which led to the conclusion that only the deep lower mantle may provide the required thermodynamic conditions for their occurrence (Binck et al. 2020b; Boulard et al. 2011, 2012, 2015; Cerantola et al. 2017; Merlini et al. 2015, 2017; Lobanov et al. 2017).

Recent theoretical studies, however, have indicated that carbonate polymorphs in the system CaO-CO_2 , which contain CO_4 -groups may be stable at pressures and temperatures corresponding to the conditions of Earth's transition zone and uppermost lower mantle (Sagatova et al. 2020; Yao et al. 2018). Specifically, Yao et al. (2018) predicted that Ca_3CO_5 -*Cmcm* and CaC_2O_5 -*Pc* may be stable phases at pressures >11 and >33 GPa, respectively, while Sagatova et al. (2020) found Ca_2CO_4 -*Pnma* to be a stable phase at pressures >13 GPa.

While the phase diagram of CaCO_3 is well constrained for

* E-mail: binck@kristall.uni-frankfurt.de

† Special collection papers can be found online at <http://www.minsocam.org/MSA/AmMin/special-collections.html>.

the pressure and temperature conditions of Earth's upper and lower mantle (Bayarjargal et al. 2018; Gavryushkin et al. 2017; Ishizawa et al. 2013; Lobanov et al. 2017; Ono et al. 2007), experimental studies focusing on different compositions in the system CaO - CO_2 have not been reported up to now. In this study, we have used a multidisciplinary experimental and theoretical approach, which allowed us to verify the formation of calcium orthocarbonate (Ca_2CO_4 -*Pnma*) at *P-T* conditions of the Earth's transition zone and lower mantle. We report the experimentally determined crystal structure of calcium orthocarbonate (Ca_2CO_4 -*Pnma*) and present the first experimental and theoretical Raman spectra of the new compound.

EXPERIMENTAL METHODS

Preparation of high-pressure, high-temperature experiments

For low-pressure and moderate-temperature Raman spectroscopy and X-ray diffraction experiments (up to ~23 GPa and ~2300 K), Boehler-Almax type (Boehler 2006) diamond-anvil cells (DAC) were employed. Raman-compatible diamonds with low birefringence, ultralow fluorescence and culets of 300–350 μm in diameter were inserted in WC seats. The opening angles of the cells were 48 and 70°, respectively. A BX-90 type DAC (Kantor et al. 2012) was used for high-pressure, high-temperature X-ray diffraction experiments (up to ~93 GPa and ~2500 K), with a 120 μm culet diamond inserted in a WC seat. Depending on the culet size, sample chambers of 60–175 μm in diameter were laser drilled in Re gaskets pre-indentated to ~15–45 μm . The diamond-anvil cells for the experiments at moderate pressures were loaded with natural CaCO_3 single crystals, surrounded by compacted CaO powder (analytical-grade chemPUR 99.95%) and ruby pressure markers. The CaCO_3 single crystals had edge lengths ranging from ~15–60 μm . Before loading, CaO and CaCO_3 were dried for 48 h at 460 °C, to remove surface moisture. The DAC employed for the high-pressure experiments was loaded with calcium azide (CaN_6) containing CaO and a nitrogen pressure-transmitting medium.

Raman spectroscopy in the LH-DAC

Raman spectra were measured at the Institute of Geosciences at the Goethe Universität Frankfurt in 0.5–4 GPa steps upon compression and decompression covering a range between ambient pressure and ~23 GPa. A frequency doubled 532.14 nm Nd:YAG Oxxius laser (LCX 532S) was focused on the sample with a spot size of 6 μm . Spectra were collected in backscattering geometry, using a grating spectrometer (Acton, SP-2356) equipped with a CCD detector (Pixis 256E) and a microscope objective (Mitutoyo). The spectral resolution of the spectrometer is 3 cm^{-1} (Bayarjargal et al. 2018). The laser power was set to 430 mW and spectra were collected for 50 s in a frequency window of 100–1500 cm^{-1} , using a grating of 1800 grooves/mm. The estimated laser power on the sample was around ~250 mW. The pressure was determined before and after the Raman measurement, using the ruby reference scales for non-hydrostatic (Mao et al. 1978) conditions. The accuracy of our pressure determination by the ruby scale was within 6%, while pressure gradients may have caused absolute uncertainties up to 3 GPa during and after laser heating.

The sample was heated from both sides with a pulsed CO_2 -laser (Diamond K-250 from Coherent, $\lambda = 10.6$ μm), reaching temperatures up to ~2300 K. For the determination we used the same setup as for the Raman measurements, while the grating was set to 150 grooves/mm. To achieve coupling of the CO_2 -laser from both sides of the sample, the laser power was set in a range between 1–6 W, depending on the pressure and the loading of the diamond-anvil cell. The heating laser was focused on the sample so that the diameter of the heated area was around 25 μm , which nearly covered all of the single crystals. We moved the heating laser across the sample, while heating for about 5 min per position. The position of the Raman laser with respect to the heated areas on the sample was controlled using an optical camera. The thermal emission of the sample, as well as the Raman signal was measured with a spatial resolution of around 5–6 μm , i.e., the areas for the measurements were significantly smaller than the heating spots. The temperatures during laser heating were determined by the two-color pyrometer method, employing Planck and Wien fits (Benedetti and Loubeyre 2004). We assume a typical uncertainty associated with radiometric temperature measurements in LH-DACs of ~10%.

High-pressure single-crystal X-ray diffraction

High pressure single-crystal X-ray diffraction (SC-XRD) data were acquired at the P02.2 and 13-IDD beamlines of PETRA III (DESY, Hamburg, Germany) and the Advanced Photon Source (APS, Chicago, U.S.A.), respectively. Two different phase assemblages were compressed up to ~20 and ~89 GPa at ambient temperature. The samples were laser-heated in a temperature range between ~1830 and ~2500 K once the cells had reached the desired pressures. The sample material of the low-pressure cell was heated using the CO_2 -laser heating system described above. The high-pressure cell was heated using the double-sided YAG laser-heating system at the 13-IDD beamline of the APS, with CaN_6 acting as the laser-absorber. Temperatures were measured using the thermal emission (Mezouar et al. 2017). The pressures inside the sample chambers were either determined using the ruby fluorescence method (Mao et al. 1978), or from the vibrational mode of the stressed diamond anvil (Akahama and Kawamura 2006).

The synthesized polycrystalline samples were characterized upon compression and decompression by SC-XRD measurements. At the P02.2 beamline, a Perkin Elmer XRD 1621 detector was employed with an X-ray beam ($\lambda = 0.2901$ Å or $\lambda = 0.2887$ Å, depending on the experiment) focused down to about 2×2 μm^2 . At the GSECARS beamline, a Pilatus CdTe 1M detector was used along with an X-ray beam ($\lambda = 0.2952$ Å) focused down to 3×3 μm^2 . On the polycrystalline samples, a full X-ray diffraction mapping of the sample chamber was performed after laser-heating to identify the most promising sample positions for a single-crystal data collection. On the locations where the most intense single-crystal reflections were detected, single-crystal data were acquired in step-scans of 0.5° from -36° to $+36^\circ$ ω and 5 s exposure time. The CrysAlisPro software [Rigaku Oxford Diffraction (Rigaku and CrysAlis 2018)] was utilized for the single-crystal data analysis. To calibrate the instrumental model in the CrysAlisPro software, i.e., the sample-to-detector distance, detector's origin, offsets of goniometer angles, and rotation of both X-ray beam and the detector around the instrument axis, a single crystal of orthoenstatite $[(\text{Mg}_{1.93}\text{Fe}_{0.06})(\text{Si}_{1.93}\text{Al}_{0.06})\text{O}_6]$, *Pbca* space group, $a = 8.8117(2)$ Å, $b = 5.18320(10)$ Å, and $c = 18.2391(3)$ Å was used. The same calibration crystal was used at all beamlines. The analysis procedure in the CrysAlisPro software includes the peak search, the removal of the diamond anvils' parasitic reflections and saturated pixels of the detector, finding reflections belonging to a unique single crystal, the unit-cell determination and the data integration and absorption corrections. The crystal structures were then solved with SHELXT structure solution program (Sheldrick 2015) using intrinsic phasing and refined within the JANA2006 software (Petříček et al. 2014). CSD 2026976 contains the crystallographic data for Ca_2CO_4 at 89 GPa (Laniel 2020). These data can be obtained free of charge from FIZ Karlsruhe via <https://www.ccdc.cam.ac.uk/structures>. Further structural data of Ca_2CO_4 at 20.1(2) GPa and 89.0(8) GPa are given in the associated CIF¹.

Density functional theory

To obtain theoretical Raman spectra, density functional perturbation theory (DFPT) calculations were performed employing the CASTEP code (Clark et al. 2005). The code is an implementation of Kohn-Sham DFT based on a plane wave basis set in conjunction with pseudopotentials. The plane wave basis set allows the achievement of numerically converged results in a straightforward manner, as the convergence is controlled by a single adjustable parameter, the plane wave cut-off, which we set to 1020 eV. The norm-conserving pseudopotentials were generated “on the fly” from the information provided in the CASTEP database. These pseudopotentials have been tested extensively for accuracy and transferability (Lejaeghere et al. 2016). All calculations employed the GGA-PBE exchange-correlation functional (Perdew et al. 1996). The Brillouin zone integrals were performed using Monkhorst-Pack grids (Monkhorst and Pack 1976) with spacings between grid points of <0.037 Å⁻¹. Geometry optimizations were defined as being converged when the energy change between iterations was $<0.5 \times 10^{-6}$ eV/atom, the maximal residual force was <0.01 eV/Å, and the maximal residual stress was <0.02 GPa. Phonon frequencies were obtained from density functional perturbation theory (DFPT) calculations. Raman intensities were computed using DFPT in the “ $2n+1$ ” theorem approach (Miwa 2011) for a powder sample. We have shown in numerous studies that the relative intensities of Raman bands for carbonates are very well reproduced and predicted with this approach (Nguyen-Thanh et al. 2016; Biedermann et al. 2017; Bayarjargal et al. 2018; Binck et al. 2020a, 2020b). Reaction enthalpies were computed in the athermal limit by comparing the sum of the enthalpies of the reactants to those of the products at prescribed pressures.

RESULTS

Crystal structure of Ca_2CO_4 -*Pnma*

Our single-crystal diffraction measurements unequivocally show the appearance of a new set of diffraction spots upon laser-

heating, which were indexed with an orthorhombic unit cell (space group *Pnma*). The structure was readily solved and refined for data sets obtained at 20.1(2) and 89.0(8) GPa (Online Materials¹). All other data sets between 10 and 93 GPa were successfully indexed with the same unit cell (Online Materials¹).

Ca_2CO_4 -*Pnma* has 28 atoms ($Z = 4$ formula units) in the unit cell and is characterized by carbon that is coordinated by oxygen fourfold, forming isolated CO_4 tetrahedra. Ca atoms occupy two non-equivalent crystallographic positions and form CaO_9 and CaO_{11} polyhedra (Fig. 1). Geometric parameters of the crystal structure at 20.1(2) and 89.0(8) GPa are listed in Table 1.

The CO_4 tetrahedra share corners, edges and faces with the CaO_{11} polyhedra, but only share corners and edges with the CaO_9 polyhedra. The CaO_9 polyhedra are irregularly shaped, while the CaO_{11} polyhedra form fivefold-capped trigonal prisms (Sagatova et al. 2020). CaO_9 and CaO_{11} polyhedra are connected via their faces. Upon compression from 20.1(2) to 89.0(8) GPa, the overall unit-cell volume decreases by $\sim 20\%$. The C-O bond lengths range from 1.378(14) to 1.386(7) Å at 20.1(2) GPa. They shorten by $\sim 3\%$ when a pressure of 89.0(8) GPa is reached [C-O bond range 1.323(16)–1.381(11) Å]. The volume of the CO_4 tetrahedra decreases by $\sim 9\%$ from 20.1(2) GPa ($V = 1.35 \text{ Å}^3$) to 89.0(8) GPa ($V = 1.23 \text{ Å}^3$). The distortion of a coordination polyhedron can be defined by an index D , with $D = 1/n \sum_{i=1}^n [(l_i - l_{\text{av}})/l_{\text{av}}]$, where l_i is the distance from the central atom to the i th coordinating atom and l_{av} is the average bond length (Baur 1974). The distortion of the CO_4 polyhedra at 20.1(2) GPa is small with $D = 0.002$, and increases only slightly to 0.015 upon pressure increase to 89.0(8) GPa. The average bond lengths of the CaO_9 and CaO_{11} coordination polyhedra decrease from 2.360 to 2.174 Å and 2.532 to 2.338 Å over the same pressure range, corresponding to a pressure-induced volume decrease of 20.8 and 20.5%, respectively.

In summary, our SC-XRD experiments demonstrated that $\text{CaO} + \text{CaCO}_3$ reacts at pressures as low as ~ 20 GPa and ~ 1830 K to form Ca_2CO_4 . Furthermore, the CaO in CaN_6 reacted with the diamond culet at ~ 89 GPa and ~ 2500 K to form Ca_2CO_4 . The new

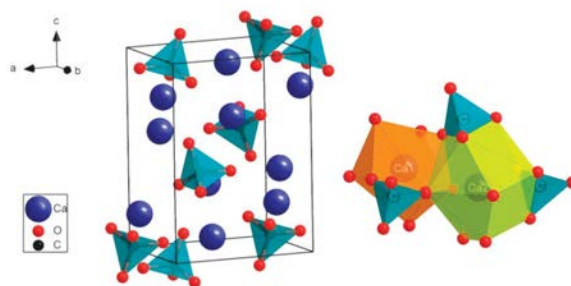


FIGURE 1. Structure of calcium orthocarbonate (Ca_2CO_4 -*Pnma*) at ~ 20 GPa. Carbon atoms appear not to be coordinated by oxygen in a threefold configuration, but form isolated CO_4 tetrahedra. The Ca atoms occupy two different sites, and they form CaO_9 (orange) and CaO_{11} (green) polyhedra. (Color online.)

TABLE 1. Structural parameters of Ca_2CO_4 -*Pnma* at 20 and 89 GPa; distances are in d (Å) and angles in \angle (°)

Pressure (GPa)	Group	Min	Max	Average
20.1(2)	$d(\text{C-O})$	1.378(14)	1.386(7)	1.383
	$\angle(\text{O-C-O})$	107.5(5)	112.9(6)	110.3
	$d(\text{Ca1-O})$	2.227(8)	2.601(2)	2.360
	$d(\text{Ca2-O})$	2.258(9)	2.893(6)	2.532
	$d(\text{C-O})$	1.323(16)	1.381(11)	1.340
89.0(8)	$\angle(\text{O-C-O})$	107.4(6)	116.0(9)	109.5
	$d(\text{Ca1-O})$	2.088(8)	2.329(4)	2.174
	$d(\text{Ca2-O})$	2.129(6)	2.559(10)	2.338

phase formed in the experiments is a calcium orthocarbonate with a structure that has recently been predicted (Sagatova et al. 2020).

We calculated structural parameters for Ca_2CO_4 -*Pnma* for pressures ranging from 0 to 100 GPa using density functional theory calculations. Our Mulliken population analysis of the C-O bonds clearly shows that all four C-O bonds in a CO_4 tetrahedron are similar, i.e., all four bonds have high populations of $\sim 0.65 e/\text{Å}^3$, indicative of covalent bonding. The calculated volume data were fitted using a third-order Birch-Murnaghan equation of state and are shown alongside experimental data (Fig. 2a). The extrapolated

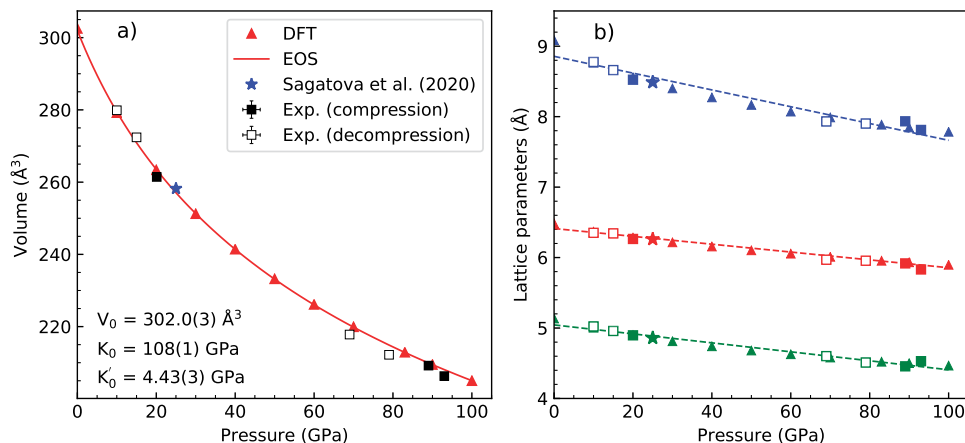


FIGURE 2. (a) Pressure-dependence of the unit-cell volume of Ca_2CO_4 -*Pnma*. The DFT data were fitted using a third-order Birch-Murnaghan EOS (Gonzalez-Platas et al. 2016; Birch 1947) using the EoS-FIT7-GUI program (Gonzalez-Platas et al. 2016). (b) Linear fits (dashed lines) to the pressure dependence of DFT lattice parameters. Colors correspond to the a (red), b (green), and c (blue) lattice parameters. Filled and open squares correspond to experimental data obtained upon compression and decompression, respectively. Filled triangles correspond to DFT-calculated data points. Stars correspond to the predicted lattice parameters of Ca_2CO_4 -*Pnma* at 25 GPa as obtained by Sagatova et al. (2020). (Color online.)

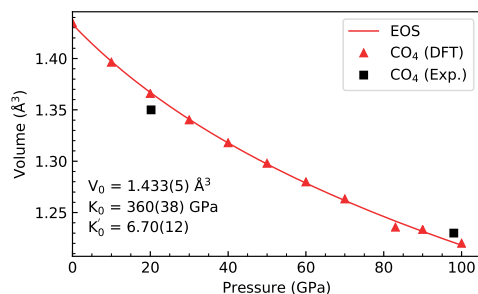


FIGURE 3. Pressure-dependence of the CO_4 tetrahedron volume of Ca_2CO_4 -*Pnma*. The DFT data were fitted using a third-order Birch-Murnaghan EOS (Gonzalez-Platas et al. 2016; Birch 1947) using the EoS-FIT7-GUI program (Gonzalez-Platas et al. 2016). (Color online.)

unit-cell volume at ambient pressure is $302.0(3) \text{ \AA}^3$ and the bulk modulus and its first pressure derivative are $K_0 = 108(1) \text{ GPa}$ and $K'_0 = 4.43(3)$, respectively. The experimentally determined unit-cell dimensions closely resemble those obtained by DFT calculations derived in this work and by Sagatova et al. (2020) (Figs. 2a and 2b). The DFT-calculated volumes of the CO_4 , CaO_9 , and CaO_{11} polyhedra were further fitted using third-order Birch-Murnaghan equations of state and are shown together with the experimental volumes of the solved crystal structures (Fig. 3 and Online Materials¹). The bulk modulus of the CO_4 groups is $360(38) \text{ GPa}$ with $K'_0 = 6.70(12)$ and $V_0 = 1.433(5) \text{ \AA}^3$. For the CaO_9 and CaO_{11} polyhedra, the bulk moduli are $99(3)$ and $106(3) \text{ GPa}$ with $K'_0 = 4.30(8)$ and $V_0 = 29.32(8)$, as well as $K'_0 = 4.31(9)$ and $40.09(11) \text{ \AA}^3$, respectively.

Experimental and theoretical Raman spectra of Ca_2CO_4 -*Pnma*

Raman spectra of $\text{CaO}+\text{CaCO}_3$ were measured upon cold compression up to $22.8(2) \text{ GPa}$. Raman signals of a sequence of metastable high-pressure polymorphs are expected when calcite is used as CaCO_3 precursor instead of aragonite (Bayarjargal et al. 2018; Koch-Müller et al. 2016). $\text{CaO-Fm}\bar{3}m$, on the other hand, is known to be Raman inactive and should not contribute to the measured signal. We obtained CaCO_3 -III at around $\sim 6 \text{ GPa}$, which eventually transformed to CaCO_3 -VI at above $\sim 15 \text{ GPa}$ (Online Materials¹). We increased the pressure to $\sim 23 \text{ GPa}$ before laser heating. When heating the CaCO_3 -VI single crystals to ~ 1830 and to $\sim 2255 \text{ K}$ in two distinct experiments, they reacted immediately with the surrounding $\text{CaO-Fm}\bar{3}m$. In both runs, the pressure after heating dropped by approximately 1.6 – 2.7 GPa . Raman spectra that have been obtained after quenching the sample to ambient temperatures show well-resolved new features (Fig. 4), which cannot be explained by the Raman spectra of CaCO_3 -VI or of aragonite (Online Materials¹ data). At $19.9(4) \text{ GPa}$, the most prominent feature of the newly synthesized phase is a strong Raman band at 996.4 cm^{-1} (Fig. 4). Furthermore, at least eight new Raman bands are observable in a range of 557 – 774 cm^{-1} , and more than 12 new modes appear in the low-frequency range between 121 – 399 cm^{-1} . We observe CaCO_3 -VI in the non-heated areas, which demonstrates the localized increase of temperature upon laser heating. In both runs, we were not able to find any evidence for the presence of aragonite, suggesting a strong reactivity in the CaO-CaCO_3 system if sufficient energy is provided.

According to group theory, 42 Raman active modes are expected

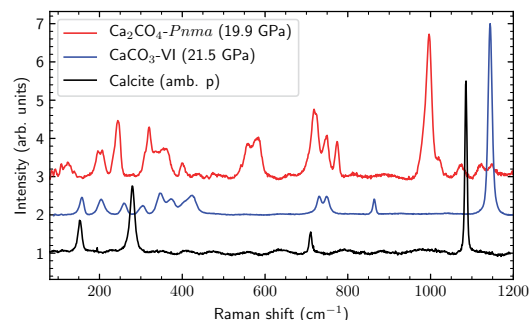


FIGURE 4. Experimental Raman spectra obtained in the CaO-CaCO_3 system. At ambient conditions, only CaCO_3 with calcite structure ($R\bar{3}c$) is Raman-active, which upon cold compression to $21.5(2) \text{ GPa}$ has the CaCO_3 -VI structure ($P\bar{1}$). After heating to $\sim 2255 \text{ K}$ and quenching to ambient temperature, CaCO_3 -VI has reacted with CaO , forming calcium orthocarbonate Ca_2CO_4 with the *Pnma* space group. (Color online.)

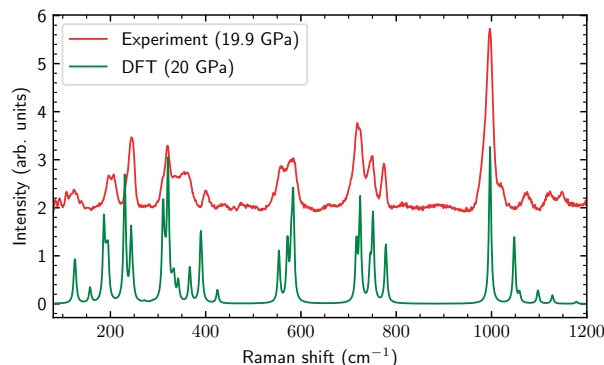


FIGURE 5. Comparison of experimental (temperature quenched from $\sim 2255 \text{ K}$) vs. theoretical Raman spectra of Ca_2CO_4 -*Pnma* at $\sim 20 \text{ GPa}$. The calculated frequencies were multiplied by a scaling factor of 1.04 . (Color online.)

for Ca_2CO_4 -*Pnma*: $\Gamma_{\text{Raman}} = 13A_g + 8B_{1g} + 13B_{2g} + 8B_{3g}$. The most prominent characteristic of Ca_2CO_4 -*Pnma* is an intra-molecular Raman band that is appearing around 1000 cm^{-1} . Raman bands in the same frequency interval have been shown to be distinctive of the intra-molecular vibrations of the CO_4 tetrahedra in CaCO_3 - $P2_1/c$ (Lobanov et al. 2017) and MgCO_3 - $C2/m$ (Binck et al. 2020b). Figure 5 demonstrates a good match between the theoretical and experimental Raman modes indicating that Ca_2CO_4 -*Pnma* is the only carbonate with sp^3 -hybridized carbon present in the sample. We observe at least 23 experimental Raman modes, which can be assigned to the theoretical spectrum at 20 GPa (Fig. 5). Missing Raman bands are due to the resolution of the spectrometer or high background of the diamonds. A calculated Raman spectrum of Ca_2CO_4 -*Pnma* at 83 GPa implies positive Grüneisen-parameters for all modes (Online Materials¹ data). According to previous calculations, Ca_2CO_4 -*Pnma* is thought to decompose below 10 GPa (Sagatova et al. 2020). We were able to acquire Raman spectra of Ca_2CO_4 -*Pnma* down to $4.1(2) \text{ GPa}$. Below that pressure the Raman spectra do not exhibit any of the characterizing features of Ca_2CO_4 anymore (Online Materials¹). Instead, at ambient conditions, a diffuse spectrum clearly showing the lattice vibrations of the CO_3 -stretching mode is present (Online Materials¹). Since the distinctive features of crystalline carbonate are absent, we infer that its amorphization has taken place due to

the cold pressure relaxation. As the decomposition may require an activation energy, the actual stability field of Ca_2CO_4 -*Pnma* currently remains unknown.

DISCUSSION AND IMPLICATIONS

Our results demonstrate that calcium orthocarbonate (Ca_2CO_4 -*Pnma*) can be formed at the *P-T* conditions of Earth's upper transition zone at ~20 GPa and ~1830 K and can persist to at least the mid-lower mantle conditions (up to ~93 GPa and ~2500 K). During the investigation of the CaO - CaCO_3 system, we neither found indications for the previously predicted Ca_3CO_5 -*Cmcm* phase and its high-pressure polymorphs (Sagatova et al. 2020; Yao et al. 2018), nor for the predicted meta-stable Ca_2CO_4 -*P2₁/m* phase (Yao et al. 2018).

Our constraints on the formation conditions of Ca_2CO_4 -*Pnma* imply that some compounds in the CaO - CO_2 system may have comparatively low-*sp*²-*sp*³ transition pressures, corresponding to lower upper mantle conditions. This stands in strong contrast to the *sp*²-*sp*³ crossover of pure CaCO_3 , which was observed at pressures >100 GPa (Lobanov et al. 2017; Oganov et al. 2006; Ono et al. 2007; Pickard and Needs 2015). Although the solubility of carbon into major mantle minerals has been shown to be low (Shcheka et al. 2006), the *sp*²-*sp*³ transition in carbonates may have a significant impact on the silicate-carbonate equilibria and thus the potential for carbonates to exist in the mantle. Such effects can now be studied in the CaO - CO_2 system at comparatively low pressures with large-volume presses.

A topological analogy of Ca_2CO_4 -*Pnma* with the silicates larnite β - Ca_2SiO_4 (Barbier and Hyde 1985) and flamite α'_1 - Ca_2SiO_4 (Rashchenko et al. 2019) has been reported (Sagatova et al. 2020). Carbon substitution of SiO_4 -groups by CO_4 -groups is, however, unlikely as the former are more voluminous by a factor of ~2 than the latter (e.g., Hugh-Jones et al. 1997; Kudo and Takéuchi 1985; Milman et al. 2001; Smyth and Bish 1988 and references therein). Also, the compressibility of isolated CO_4 tetrahedra (K_0 ~360 GPa) is lower than that of SiO_4 tetrahedra (K_0 ~300 GPa), which, based on crystal-chemical considerations, is the expected behavior due to the smaller cation radius of C. However, it is now worthwhile to explore the phase stabilities of compounds in which CO_4 groups and SiO_6 -octahedra may coexist.

We investigated whether *sp*³-hybridized calcium orthocarbonate can coexist with silicates in the mantle. While at the *P-T* conditions of the transition zone and upper lower mantle, CaCO_3 + SiO_2 were shown to form CaSiO_3 + CO_2 (Li et al. 2018), our DFT-calculations at 20, 30, and 40 GPa show, that Ca_2CO_4 + 2SiO_2 are more stable than 2CaSiO_3 + CO_2 (Fig. 6). This implies that Ca_2CO_4 -*Pnma* could exist together with silica at the *P-T* conditions of the transition zone and upper lower mantle. In fact, the presence of CaCO_3 inclusions in super deep diamonds derived from the transition zone or the lower mantle (Brenker et al. 2007; Kaminsky et al. 2016) is inconsistent with the assumption that CaCO_3 will always react with the surrounding mantle.

Isotopic signatures (Harte 2010; Tappert et al. 2005) and carbonate inclusions in diamonds (Brenker et al. 2007; Kaminsky et al. 2016) suggest that diamonds may form during “redox freezing,” i.e., when the oxidized carbonate-bearing subducting slab has reached the more reduced transition zone or the lower mantle, and releases carbonate and/or carbonatitic melts, which reduce oxidized carbon

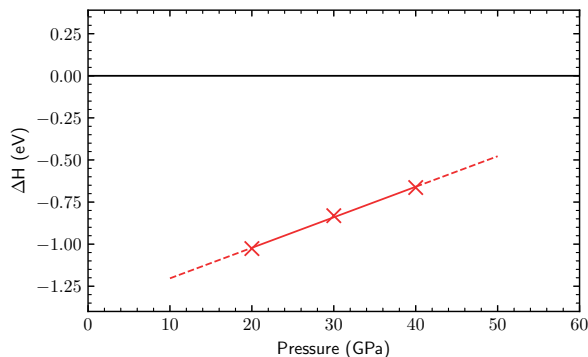


FIGURE 6. Pressure-dependence of the reaction enthalpy ΔH for the reaction $\text{Ca}_2\text{CO}_4 + 2\text{SiO}_2 \rightleftharpoons 2\text{CaSiO}_3 + \text{CO}_2$. Negative values indicate that the phase assemblage on the left-hand side of the equation is stable. Crosses represent calculated values, the solid red line is a linear fit to these values, while the dashed red line indicates an extrapolation. The values plotted are for CO_2 -V and orthorhombic CaSiO_3 -perovskite. Using either CO_2 -III or CO_2 -IV (Han et al. 2019; Lu et al. 2013) would stabilize Ca_2CO_4 further by ~0.2 eV. The enthalpy difference between cubic and orthorhombic CaSiO_3 (Caracas et al. 2005, 2006; Komabayashi et al. 2007) is negligible in the present context. (Color online.)

to diamond (Rohrbach and Schmidt 2011; Stagno et al. 2013). The inverse scenario called “redox melting” occurs when reduced carbon-bearing rocks are lifted up above the 660 km discontinuity of the transition zone due to the upwelling mantle (Rohrbach and Schmidt 2011; Stagno et al. 2013). In this case, carbonate and/or carbonatitic melts form due to reoxidation of diamond. Our results show that Ca_2CO_4 -*Pnma* may form during such redox processes. Diamonds that have formed during redox melting could initially conserve calcium orthocarbonate. These orthocarbons would transform or decompose once the diamond is elevated above the base of thick continental crust and could then only be identified by the decomposition products. Indications of the presence of calcium-bearing inclusions such as CaO , CaF_2 , and $\text{Ca}(\text{OH})_2$ in diamond have been found in the presence of CO_3 -groups (Dobrzhinetskaya et al. 2007). Such a phase assemblage would be consistent with the expected remnants of decomposed Ca_2CO_4 -*Pnma*.

ACKNOWLEDGMENTS

The authors acknowledge funding by the Deutsche Forschungsgemeinschaft (DFG)-Germany (FOR2125/CarboPaT, BA4020, WI1232). The “2n + 1” Raman theorem in CASTEP was developed under grant EP/I030107/1. D.L. thanks the Alexander von Humboldt Foundation for financial support. DESY (Hamburg, Germany), a member of the Helmholtz Association (HGF) is acknowledged for the provision of experimental facilities. Portions of this work were performed at GeoSoilEnviroCARS (The University of Chicago, Sector 13), Advanced Photon Source (APS), Argonne National Laboratory. GeoSoilEnviroCARS is supported by the National Science Foundation - Earth Sciences (EAR - 1634415) and Department of Energy-GeoSciences (DE-FG02-94ER14466). This research used resources of the Advanced Photon Source, a U.S. Department of Energy (DOE) Office of Science User Facility operated for the DOE Office of Science by Argonne National Laboratory under Contract No. DE-AC02-06CH11357.

REFERENCES CITED

- Akahama, Y., and Kawamura, H. (2006) Pressure calibration of diamond anvil Raman gauge to 310 GPa. *Journal of Applied Physics*, 100, 043516.
- Barbier, J., and Hyde, B. (1985) The structures of the polymorphs of dicalcium silicate, Ca_2SiO_4 . *Acta Crystallographica*, B41, 383–390.
- Baur, W. (1974) The geometry of polyhedral distortions. Predictive relationships for the phosphate group. *Acta Crystallographica*, B30, 1195–1215.
- Bayarjargal, L., Fröhner, C.-J., Schrödt, N., and Winkler, B. (2018) CaCO_3 phase

- diagram studied with Raman spectroscopy at pressures up to 50 GPa and high temperatures and DFT modeling. *Physics of the Earth and Planetary Interiors*, 281, 31–45.
- Benedetti, L.R., and Loubeyre, P. (2004) Temperature gradients, wavelength-dependent emissivity, and accuracy of high and very-high temperatures measured in the laser-heated diamond cell. *High Pressure Research*, 24, 423–445.
- Biedermann, N., Speziale, S., Winkler, B., Reichmann, H.J., Koch-Müller, M., and Heide, G. (2017) High-pressure phase behavior of SrCO_3 : an experimental and computational Raman scattering study. *Physics and Chemistry of Minerals*, 44, 335–343.
- Binck, J., Chariton, S., Stekiel, M., Bayarjargal, L., Morgenroth, W., Milman, V., Dubrovinsky, L., and Winkler, B. (2020a) High-pressure, high-temperature phase stability of iron-poor dolomite and the structures of dolomite-IIIc and dolomite-V. *Physics of the Earth and Planetary Interiors*, 299, 106403.
- Binck, J., Bayarjargal, L., Lobanov, S.S., Morgenroth, W., Luchitskaia, R., Pickard, C.J., Milman, V., Refson, K., Jochym, D.B., Byrne, P., and Winkler, B. (2020b) Phase stabilities of MgCO_3 and MgCO_3 -II studied by Raman spectroscopy, X-ray diffraction, and density functional theory calculations. *Physical Review Materials*, 4, 055001.
- Birch, F. (1947) Finite elastic strain of cubic crystals. *Physical Review*, 71, 809–824.
- Boehler, R. (2006) New diamond cell for single-crystal X-ray diffraction. *Review of Scientific Instruments*, 77, 115103.
- Boulard, E., Gloter, A., Corgne, A., Antonangeli, D., Auzende, A.L., Perrillat, J.P., Guyot, F., and Fiquet, G. (2011) New host for carbon in the deep Earth. *Proceedings of the National Academy of Sciences*, 108, 5184–5187.
- Boulard, E., Menguy, N., Auzende, A.L., Benzerara, K., Bureau, H., Antonangeli, D., Corgne, A., Morard, G., Siebert, J., Perrillat, J.P., Guyot, F., and Fiquet, G. (2012) Experimental investigation of the stability of Fe-rich carbonates in the lower mantle. *Journal of Geophysical Research: Solid Earth*, 117.
- Boulard, E., Pan, D., Galli, G., Liu, Z., and Mao, W.L. (2015) Tetrahedrally coordinated carbonates in Earth's lower mantle. *Nature Communications*, 6, 6311.
- Brenker, F.E., Vollmer, C., Vincze, L., Vekemans, B., Szymanski, A., Janssens, K., Szaloki, I., Nasdala, L., Joswig, W., and Kaminsky, F. (2007) Carbonates from the lower part of transition zone or even the lower mantle. *Earth and Planetary Science Letters*, 260, 1–9.
- Caracas, R., and Wentzcovitch, R.M. (2006) Theoretical determination of the structures of CaSiO_3 perovskites. *Acta Crystallographica*, B62, 1025–1030.
- Caracas, R., Wentzcovitch, R., Price, G.D., and Brodholt, J. (2005) CaSiO_3 perovskite at lower mantle pressures. *Geophysical Research Letters*, 32.
- Cerantola, V., Bykova, E., Kuppenko, I., Merlini, M., Ismailova, L., McCammon, C., Bykov, M., Chumakov, A.I., Petitgirard, S., Kantor, I., and others (2017) Stability of iron bearing carbonates in the deep Earth's interior. *Nature Communications*, 8, 15960.
- Chariton, S., Bykov, M., Bykova, E., Koemets, E., Fedotenko, T., Winkler, B., Hanfland, M., Prakashenka, V.B., Greenberg, E., McCammon, C., and Dubrovinsky, L. (2020) The crystal structures of Fe-bearing MgCO_3 sp^2 - and sp^3 -carbonates at 98 GPa from single-crystal X-ray diffraction using synchrotron radiation. *Acta Crystallographica. Section E, Crystallographic Communications*, 76, 715–719.
- Clark, S.J., Segall, M.D., Pickard, C.J., Hasnip, P.J., Probert, M.I., Refson, K., and Payne, M.C. (2005) First principles methods using CASTEP. *Zeitschrift für Kristallographie, Crystalline Materials*, 220, 567–570.
- Clift, P.D. (2017) A revised budget for Cenozoic sedimentary carbon subduction. *Reviews of Geophysics*, 55, 97–125.
- Dobrzynetskaia, L.F., Wirth, R., and Green, H.W. (2007) A look inside of diamond-forming media in deep subduction zones. *Proceedings of the National Academy of Sciences*, 104, 9128–9132.
- Gavryushkin, P.N., Martirosyan, N.S., Inerbaev, T.M., Popov, Z.I., Rashchenko, S.V., Likhacheva, A.Y., Lobanov, S.S., Goncharov, A.F., Prakashenka, V.B., and Litasov, K.D. (2017) Aragonite-II and CaCO_3 -VII: New high pressure, high-temperature polymorphs of CaCO_3 . *Crystal Growth & Design*, 17, 6291–6296.
- Gonzalez-Platas, J., Alvaro, M., Nestola, F., and Angel, R.J. (2016) EosFit7-GUI: A new GUI tool for equation of state calculations, analyses and teaching. *Journal of Applied Crystallography*, 49, 1377–1382.
- Han, Y., Liu, J., Huang, L., He, X., and Li, J. (2019) Predicting the phase diagram of solid carbon dioxide at high pressure from first principles. *npj Quantum Materials*, 4, 1–7.
- Harte, B. (2010) Diamond formation in the deep mantle: The record of mineral inclusions and their distribution in relation to mantle dehydration zones. *Mineralogical Magazine*, 74, 189–215.
- Hirschmann, M.M. (2018) Comparative deep earth volatile cycles: The case for C recycling from exosphere/mantle fractionation of major (H_2O , C, N) volatiles and from H_2O /Ce, CO_2 /Ba, and CO_2 /Nb exosphere ratios. *Earth and Planetary Science Letters*, 502, 262–273.
- Hugh-Jones, D., Chopelas, A., and Angel, R. (1997) Tetrahedral compression in $(\text{Mg,Fe})\text{SiO}_3$ orthopyroxenes. *Physics and Chemistry of Minerals*, 24, 301–310.
- Ishizawa, N., Setoguchi, H., and Yanagisawa, K. (2013) Structural evolution of calcite at high temperatures: Phase V unveiled. *Scientific Reports*, 3, 2832.
- Kaminsky, F.V., Ryabchikov, I.D., and Wirth, R. (2016) A primary natrocarbonatitic association in the Deep Earth. *Mineralogy and Petrology*, 110, 387–398.
- Kantor, I., Prakashenka, V., Kantor, A., Dera, P., Kurnosov, A., Sinogeikin, S., Dubrovinskaya, N., and Dubrovinsky, L. (2012) BX90: A new diamond anvil cell design for X-ray diffraction and optical measurements. *The Review of Scientific Instruments*, 83, 125102.
- Kelemen, P.B., and Manning, C.E. (2015) Reevaluating carbon fluxes in subduction zones, what goes down, mostly comes up. *Proceedings of the National Academy of Sciences*, 112, E3997–E4006.
- Koch-Müller, M., Jahn, S., Birkholz, N., Ritter, E., and Schade, U. (2016) Phase transitions in the system CaCO_3 at high P and T determined by in situ vibrational spectroscopy in diamond anvil cells and first-principles simulations. *Physics and Chemistry of Minerals*, 43, 545–561.
- Komabayashi, T., Hirose, K., Sata, N., Ohishi, Y., and Dubrovinsky, L.S. (2007) Phase transition in CaSiO_3 perovskite. *Earth and Planetary Science Letters*, 260, 564–569.
- Kudoh, Y., and Takéuchi, Y. (1985) The crystal structure of forsterite Mg_2SiO_4 under high pressure up to 149 kb. *Zeitschrift für Kristallographie, Crystalline Materials*, 171, 291–302.
- Laniel, D. (2020) CCDC 2026976: Experimental Crystal Structure Determination. CCDC, FIZ Karlsruhe. DOI: 10.5517/ccdc.csd.cc2617bv.
- Lejaeghere, K., Bihlmayer, G., Björkman, T., Blaha, P., Blügel, S., Blum, V., Caliste, D., Castelli, I.E., Clark, S.J., Dal Corso, A., and others (2016) Reproducibility in density functional theory calculations of solids. *Science*, 351, aad3000.
- Li, X., Zhang, Z., Lin, J.-F., Ni, H., Prakashenka, V.B., and Mao, Z. (2018) New high-pressure phase of CaCO_3 at the topmost lower mantle: Implication for the deep-mantle carbon transportation. *Geophysical Research Letters*, 45, 1355–1360.
- Lobanov, S.S., Dong, X., Martirosyan, N.S., Samtsevich, A.I., Stevanovic, V., Gavryushkin, P.N., Litasov, K.D., Greenberg, E., Prakashenka, V.B., Oganov, A.R., and Goncharov, A.F. (2017) Raman spectroscopy and X-ray diffraction of sp^3 CaCO_3 at lower mantle pressures. *Physical Review B*, 96, 104101.
- Lu, C., Miao, M., and Ma, Y. (2013) Structural evolution of carbon dioxide under high pressure. *Journal of the American Chemical Society*, 135, 14167–14171.
- Maeda, F., Ohtani, E., Kamada, S., Sakamaki, T., Hirao, N., and Ohishi, Y. (2017) Diamond formation in the deep lower mantle: A high-pressure reaction of MgCO_3 and SiO_2 . *Scientific Reports*, 7, 40602.
- Mao, H., Bell, P., Shaner, J.T., and Steinberg, D. (1978) Specific volume measurements of Cu, Mo, Pd, and Ag and calibration of the ruby R1 fluorescence pressure gauge from 0.06 to 1 Mbar. *Journal of Applied Physics*, 49, 3276–3283.
- Martirosyan, N., Yoshino, T., Shatskiy, A., Chanyshiev, A., and Litasov, K. (2016) The CaCO_3 -Fe interaction: Kinetic approach for carbonate subduction to the deep Earth's mantle. *Physics of the Earth and Planetary Interiors*, 259, 1–9.
- McKenzie, N.R., Horton, B.K., Loomis, S.E., Stockli, D.F., Planavsky, N.J., and Lee, C.-T.A. (2016) Continental arc volcanism as the principal driver of icehouse-greenhouse variability. *Science*, 352, 444–447.
- Merlini, M., Hanfland, M., Salamat, A., Petitgirard, S., and Müller, H. (2015) The crystal structures of $\text{Mg}_2\text{Fe}_2\text{C}_2\text{O}_{13}$, with tetrahedrally coordinated carbon, and $\text{Fe}_{13}\text{O}_{19}$, synthesized at deep mantle conditions. *American Mineralogist*, 100, 2001–2004.
- Merlini, M., Cerantola, V., Gatta, G.D., Gemmi, M., Hanfland, M., Kuppenko, I., Lotti, P., Müller, H., and Zhang, L. (2017) Dolomite-IV: Candidate structure for a carbonate in the Earth's lower mantle. *American Mineralogist*, 102, 1763–1766.
- Mezour, M., Giampaoli, R., Garbarino, G., Kantor, I., Dewaele, A., Weck, G., Boccato, S., Svitlyk, V., Rosa, A., Torchio, R., Mathon, O., Hignette, O., and Bauchau, S. (2017) Methodology for in situ synchrotron X-ray studies in the laser heated diamond anvil cell. *High Pressure Research*, 37, 170–180.
- Milman, V., Akhmatkaya, E., Nobes, R., Winkler, B., Pickard, C., and White, J. (2001) Systematic ab initio study of the compressibility of silicate garnets. *Acta Crystallographica*, B57, 163–177.
- Miwa, K. (2011) Prediction of raman spectra with ultrasoft pseudopotentials. *Physical Review B*, 84, 094304.
- Monkhorst, H.J., and Pack, J.D. (1976) Special points for Brillouin-zone integrations. *Physical Review B*, 13, 5188–5192.
- Nguyen-Thanh, T., Bosak, A., Bauer, J.D., Luchitskaia, R., Refson, K., Milman, V., and Winkler, B. (2016) Lattice dynamics and elasticity of SrCO_3 . *Journal of Applied Crystallography*, 49, 1982–1990.
- Oganov, A.R., Glass, C.W., and Ono, S. (2006) High-pressure phases of CaCO_3 : Crystal structure prediction and experiment. *Earth and Planetary Science Letters*, 241, 95–103.
- Ono, S., Kikegawa, T., and Ohishi, Y. (2007) High-pressure transition of CaCO_3 . *American Mineralogist*, 92, 1246–1249.
- Palyanov, Y.N., Bataleva, Y.V., Sokol, A.G., Borzdov, Y.M., Kupriyanov, I.N., Reutsky, V.N., and Sobolev, N.V. (2013) Mantle-slab interaction and redox mechanism of diamond formation. *Proceedings of the National Academy of Sciences*, 110, 20408–20413.
- Perdew, J.P., Burke, K., and Ernzerhof, M. (1996) Generalized gradient approximation made simple. *Physical Review Letters*, 77, 3865–3868.

- Petříček, V., Dušek, M., and Palatinus, L. (2014) Crystallographic computing system JANA2006: General features. *Zeitschrift für Kristallographie, Crystalline Materials*, 229, 345–352.
- Pickard, C.J., and Needs, R.J. (2015) Structures and stability of calcium and magnesium carbonates at mantle pressures. *Physical Review B*, 91, 104101.
- Rashchenko, S.V., Seryotkin, Y.V., Sokol, E.V., and Kokh, S.N. (2019) Incommensurately modulated crystal structure of flamite-natural analogue of α'_H - Ca_2SiO_4 . *Acta Crystallographica*, B75, 1137–1143.
- Ridgwell, A. (2005) A Mid Mesozoic revolution in the regulation of ocean chemistry. *Marine Geology*, 217, 339–357.
- Rigaku, O.D., and CrysAlis, P.R.O. (2018) Rigaku Oxford Diffraction. Yarnton, England.
- Rohrbach, A., and Schmidt, M.W. (2011) Redox freezing and melting in the Earth's deep mantle resulting from carbon-iron redox coupling. *Nature*, 472, 209–212.
- Sagatova, D., Shatskiy, A., Sagatov, N., Gavryushkin, P.N., and Litasov, K.D. (2020) Calcium orthocarbonate, Ca_2CO_4 -*Pnma*: A potential host for subducting carbon in the transition zone and lower mantle. *Lithos*, 370–371, 105637.
- Shekha, S.S., Wiedenbeck, M., Frost, D.J., and Keppler, H. (2006) Carbon solubility in mantle minerals. *Earth and Planetary Science Letters*, 245, 730–742.
- Sheldrick, G.M. (2015) SHELXT - Integrated space-group and crystal structure determination. *Acta Crystallographica*, A71, 3–8.
- Smyth, J.R., and Bish, D.L. (1988) Crystal Structures and Cation Sites of the Rock-Forming Minerals. Allen & Unwin, p. 332.
- Stagno, V., Tange, Y., Miyajima, N., McCammon, C., Irifune, T., and Frost, D. (2011) The stability of magnesite in the transition zone and the lower mantle as function of oxygen fugacity. *Geophysical Research Letters*, 38.
- Stagno, V., Ojwang, D.O., McCammon, C.A., and Frost, D.J. (2013) The oxidation state of the mantle and the extraction of carbon from Earth's interior. *Nature*, 493, 84–88.
- Tappert, R., Stachel, T., Harris, J.W., Muehlenbachs, K., Ludwig, T., and Brey, G.P. (2005) Subducting oceanic crust: The source of deep diamonds. *Geology*, 33, 565–568.
- Wallmann, K. (2001) Controls on the Cretaceous and Cenozoic evolution of seawater composition, atmospheric CO_2 and climate. *Geochimica et Cosmochimica Acta*, 65, 3005–3025.
- Walter, M.J., Kohn, S.C., Araujo, D., Bulanova, G.P., Smith, C.B., Gaillou, E., Wang, J., Steele, A., and Shirey, S.B. (2011) Deep mantle cycling of oceanic crust: Evidence from diamonds and their mineral inclusions. *Science*, 334, 54–57.
- Yao, X., Xie, C., Dong, X., Oganov, A.R., and Zeng, Q. (2018) Novel high-pressure calcium carbonates. *Physical Review B*, 98, 014108.

MANUSCRIPT RECEIVED OCTOBER 27, 2020

MANUSCRIPT ACCEPTED FEBRUARY 17, 2021

MANUSCRIPT HANDLED BY ELIZABETH C. THOMPSON

Endnote:

¹Deposit item AM-22-37872, Online Materials. Deposit items are free to all readers and found on the MSA website, via the specific issue's Table of Contents (go to http://www.minsocam.org/MSA/AmMin/TOC/2022/Mar2022_data/Mar2022_data.html). The CIF has been peer reviewed by our Technical Editors.